Supplementary information: Ice-nucleating particles in Greenlandic glacial outwash plains

Nora Bergner[1], Grace Marsh[2], Kevin Barry[3], Larissa Lacher[4], Alexander Böhmländer[4], Joanna Alden[1,a], Carina Ahlqvist[1], Ianina Altshuler[2], Lisa Bröder[5], Daniel Farinotti[6,7], Lionel Favre[1], Coline Guillosson[1], Benjamin Heutte[1], Kristina Höhler[4], Roman Pohorsky[1], Julian Weng[8], Julia Schmale[1]

[1]Extreme Environments Research Laboratory, École Polytechnique Fédérale de Lausanne (EPFL) Valais Wallis, Sion, Switzerland.
[2]Microbiome Adaptation to the Changing Environment Laboratory, École Polytechnique Fédérale de Lausanne (EPFL) Valais Wallis, Sion, Switzerland.
[3]Department of Atmospheric Science, Colorado State University, Fort Collins, USA.
[4]Institute of Meteorology and Climate Research Atmospheric Aerosol Research (IMKAAF), Karlsruhe Institute of Technology (KIT), Karlsruhe, Germany.
[5]Department of Earth and Planetary Sciences, ETH Zürich, Zürich, Switzerland.
[6]Laboratory of Hydraulics, Hydrology and Glaciology (VAW), ETH Zürich, Zürich, Switzerland
[7]Swiss Federal Institute for Forest, Snow and Landscape Research WSL, Sion, Switzerland
[8]Laboratory of Atmospheric Chemistry, Paul Scherrer Institute, Villigen, 5232, Switzerland
[a]now at: Université Savoie Mont Blanc, INRAE, CARRTEL, Thonon-les-Bains, France

Correspondence to: Julia Schmale (julia.schmale@epfl.ch)

S1. Additional tables and figures

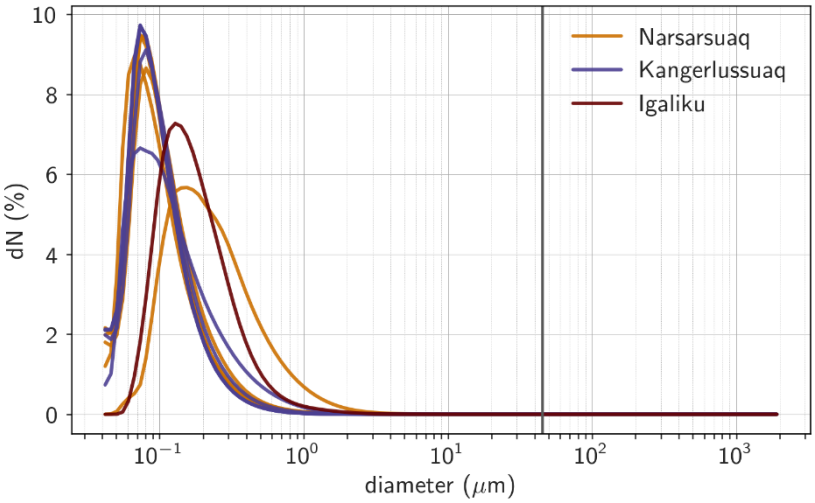

Figure S1. Dust sample grain size distributions. Particle number size distribution of *transect* dust samples from the Narsarsarsuaq, Kangerlussuaq, and Igaliku glacial outwash plains as measured with the laser diffraction particle size analyzer (0.017–2000 µm, LS 13 320, Beckman Coulter, USA). The samples have been sieved to < 45 µm (grey vertical line) for INP measurements.

Table S1. Overview of bulk dust samples. INP treatments refer to heat and hydrogen peroxide treatments for compositional information (Sect. 2.2). Additional analyses refer to ancillary measurements (Sect. 2.3) including total organic carbon (TOC), X-ray diffraction (XRD), and microbial abundance based on flow cytometry (FC) and colony forming units (CFU). For the transect samples, the geometric specific surface area (SSA_{geo}), estimated from laser diffraction particle size distributions assuming spherical particles with a density of 2650 kg m^{-3}, is provided.

Location	Sampling set	ID	Latitude (°)	Longitude (°)	Date (YYYY-MM-DD)	Description	INP treatments	Additional analyses	SSA_{geo} (m^2 g^{-1})
Narsarsuaq	transect	N1	61.220991	-45.306142	2023-07-17	dust on glacier	heat, H_2O_2	TOC, XRD	0.97
		N2	61.200598	-45.328784	2023-06-25	outwash plain	heat	TOC	1.46
		N3	61.198341	-45.330013	2023-06-20	dust deposit near river bed	heat	TOC	1.01
		N4	61.194188	-45.356143	2023-06-25	small sand dune	heat, H_2O_2	TOC	0.98
		N5	61.190831	-45.368287	2023-06-25	dust deposits near river bed	heat, H_2O_2	TOC, XRD	0.80
		N6	61.196204	-45.379716	2023-06-25	outwash plain	heat	TOC	0.54
		N7	61.173301	-45.397706	2023-06-23	dust deposits near river bed	heat	TOC	0.75
		N8	61.170274	-45.413717	2023-06-23	dust deposits near river bed	heat	TOC	-
		N9	61.167508	-45.444936	2023-06-23	dust at outflow to fjord	heat	TOC	1.01
Narsarsuaq	micro-biology	N1AT	61.207152	-45.329376	2024-07-05	unvegetated	heat	TOC, FC, CFU	- -
		N1BT	61.206739	-45.329335	2024-07-05	unvegetated	no treatments	TOC, FC, CFU	-
		N1ET	61.203417	-45.327393	2024-07-05	sparsely vegetated	heat	TOC, FC, CFU	-
		N1FT	61.203136	-45.327403	2024-07-05	vegetated	no treatments	TOC, FC, CFU	-
		N1GT	61.202204	-45.326349	2024-07-05	vegetated	heat	TOC, FC, CFU	-
		N1IT	61.202012	-45.326524	2024-07-05	vegetated	no treatments	TOC, FC, CFU	-
		N2AT	61.194997	-45.358292	2024-07-08	unvegetated	no treatments	TOC, FC, CFU	-

		N2CT	61.194518	-45.3586	2024-07-08	unvegetated	heat	TOC, FC, CFU	-
		N2ET	61.194349	-45.358387	2024-07-08	sparsely vegetated	heat	TOC, FC, CFU	-
		N2GT	61.194064	-45.357687	2024-07-08	sparsely vegetated	heat	TOC, FC, CFU	-
Kanger-lussuaq	transect	K1	67.151944	-50.0405	2023-07-07	dust on glacier	heat	TOC, XRD	0.90
		K2	67.110861	-50.194083	2023-07-07	river bank	heat, H_2O_2	TOC	1.29
		K3	67.067806	-50.355556	2023-07-07	river bank	heat, H_2O_2	TOC	1.31
		K4	67.058083	-50.397278	2023-07-07	river bank	heat	TOC, XRD	1.26
		K5	67.003917	-50.687833	2023-07-07	river bank	heat	TOC	1.52
	micro-biology	K1AT	67.089284	-50.240169	2024-07-12	unvegetated	heat	TOC, FC, CFU	-
		K1ET	67.089631	-50.240629	2024-07-12	sparsely vegetated	heat	TOC, FC, CFU	-
		K1IT	67.089500	-50.240506	2024-07-12	sparsely vegetated	heat	TOC, FC, CFU	-
		K2AT	67.066776	-50.352532	2024-07-13	unvegetated	heat	TOC, FC, CFU	-
		K2ET	67.06729	-50.352299	2024-07-13	sparsely vegetated	heat	TOC, FC, CFU	-
		K2HT	67.067879	-50.353181	2024-07-13	vegetated	heat	TOC, FC, CFU	-
Igaliku	transect	I1	60.97159	-45.052219	2023-05-28		heat, H_2O_2	TOC, XRD	1.20
		I2	60.90985	-45.234064	2023-05-31		heat	TOC	-

Figure S2. Photos of samples and stations. Example photos of (a) *transect* and (b) *microbiology* samples (the diameter of the ring is 24 cm). (c) Atmospheric stations at Narsarsuaq plain, col, Narsaq International Research station (NIRS), and Tasigaaq hill near Narsaq.

Table S2. Overview of filter samples collected for INP measurements.

Location	Latitude (°)	Longitude (°)	Altitude (m a.s.l.)	Sample ID	Filter samples start date	Filter samples end date	Total volume sampled on filter (L)
Narsarsuaq plain (*plain*)	61.20032	-45.32882	25	NUP2	2023-06-17 13:32	2023-06-18 12:01	12516
				NUP3	2023-06-18 13:17	2023-06-19 12:24	13893
				NUP4	2023-06-19 16:10	2023-06-20 11:48	10093
				NUP6	2023-06-21 15:50	2023-06-22 11:54	11093
				NUP7	2023-06-22 12:30	2023-06-23 13:11	13301
				NUP8	2023-06-23 13:34	2023-06-24 11:48	12408
				NUP9	2023-06-24 12:19	2023-06-25 10:09	8144
				NUP10	2023-06-25 10:16	2023-06-26 06:53	10491
				NUP11	2023-06-26 07:03	2023-06-27 13:47	15127
				NUP12	2023-06-27 14:13	2023-06-28 09:52	10001
				NUP13	2023-06-28 10:28	2023-07-05 17:43	103681
				NUP15	2023-07-17 16:17	2023-08-02 09:08	143463
				NUP16	2023-08-02 09:42	2023-08-09 17:29	78367
Narsarsuaq col (*col*)	61.2061254	-45.3118504	300	NUC1	2023-06-16 17:56	2023-06-19 16:41	30543
				NUC3	2023-06-21 12:53	2023-06-23 14:27	20791
				NUC4	2023-06-23 15:54	2023-06-26 07:34	38192
				NUC5	2023-06-26 07:39	2023-06-28 12:14	21653
				NUC6	2023-06-28 12:15	2023-07-05 19:02	60837
				NUC7	2023-07-05 19:50	2023-07-17 16:57	171071
				NUC8	2023-07-17 17:12	2023-08-02 10:26	132931
				NUC9	2023-08-02 11:52	2023-08-09 18:08	104540
Narsaq International Research Station (*NIRS*)	60.9157503	-46.053326	17	NA3	2023-06-27 17:15	2023-06-29 12:18	8943
				NA4	2023-06-29 12:20	2023-07-02 14:36	16373
				NA5	2023-07-02 14:40	2023-07-06 15:58	7667
				NA7	2023-07-08 10:15	2023-07-10 12:17	14847
				NA8	2023-07-10 12:21	2023-07-12 10:00	11970
				NA9	2023-07-12 10:05	2023-07-14 11:42	25886
				NA10	2023-07-14 11:45	2023-07-16 17:06	30619
				NA11	2023-07-16 17:11	2023-07-19 10:41	36030
				NA13	2023-07-19 10:48	2023-07-21 13:26	37431
				NA14	2023-07-21 13:32	2023-07-23 10:37	26658

Tasigaaq hill near Narsaq (*hill*)	60.9210617	-46.0274668	372	T1	2023-06-23 16:57	2023-06-25 18:57	18276
				T4	2023-06-27 16:03	2023-06-29 12:51	16963
				T7	2023-07-02 10:16	2023-07-04 09:59	28583
				T10	2023-07-08 17:38	2023-07-10 16:23	17709
				T15	2023-07-16 12:09	2023-07-19 11:56	20697
				T17	2023-07-21 14:58	2023-07-23 09:21	14707
				T21	2023-07-27 15:13	2023-07-30 11:44	21260

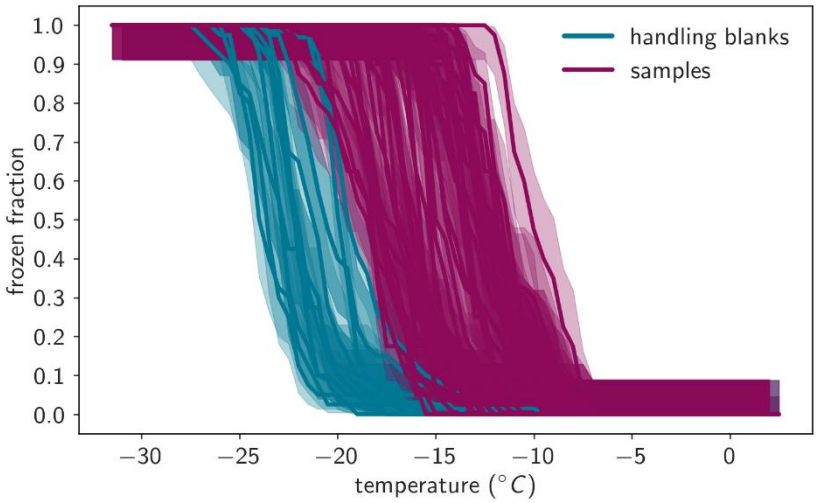

Figure S3. Comparison of frozen fraction of handling blanks and samples. Note that the washing water volume for handling blanks was 8 mL, and for filter samples 12 mL.

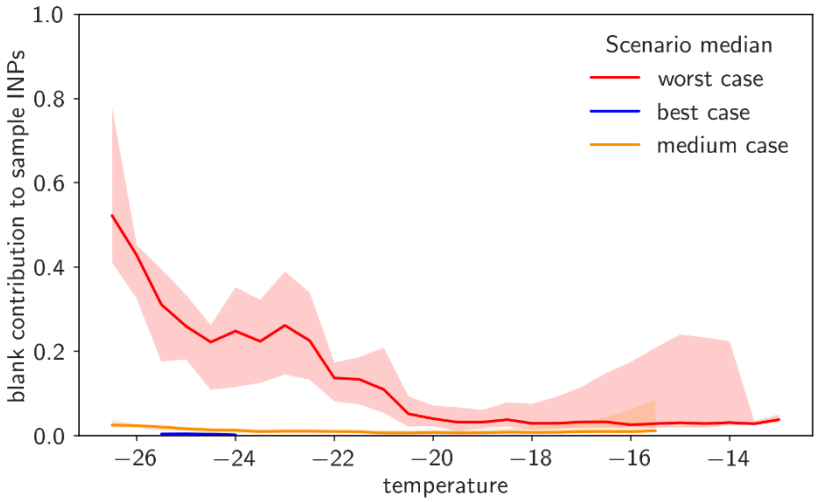

Figure S4. Contribution of procedural blank to sample INP concentrations. The fraction of procedural blank to sample INP concentrations ($N_{INP,\ procedural\ blanks}(T)$ / $N_{INP,\ samples}(T)$) is shown for three scenarios: worst case (procedural blank with maximum INP concentrations), medium case (polynomial fit to all procedural blanks), and best case (procedural blank with minimum INP concentrations). Shaded envelopes show the interquartile range across all samples, bold lines show the median.

Table S3. Mineral abundances. Phase fractions of known ice-nucleating minerals in a subset of dust samples. The phase fractions are based on XRD measurements and reported in weight percent. Refinements were conducted both with (left of /) and without (right of /) correction for preferred orientation of crystallites, the correction using spherical harmonics.

Location	Sample	Quartz (%)	Albite (%)	K-Feldspar (%)	Illite (%)
Narsarsuaq	N1	11 / 23	62 / 35	16 / 22	1 / 9
Narsarsuaq	N5	11 / 22	61 / 34	16 / 21	2 / 7
Kangerlussuaq	K1	8 / 12	52 / 49	28 / 25	4 / 4
Kangerlussuaq	K4	8 / 8	48 / 46	26 / 29	4 / 5
Igaliku	I1	7 / 9	56 / 53	20 / 22	3 / 4

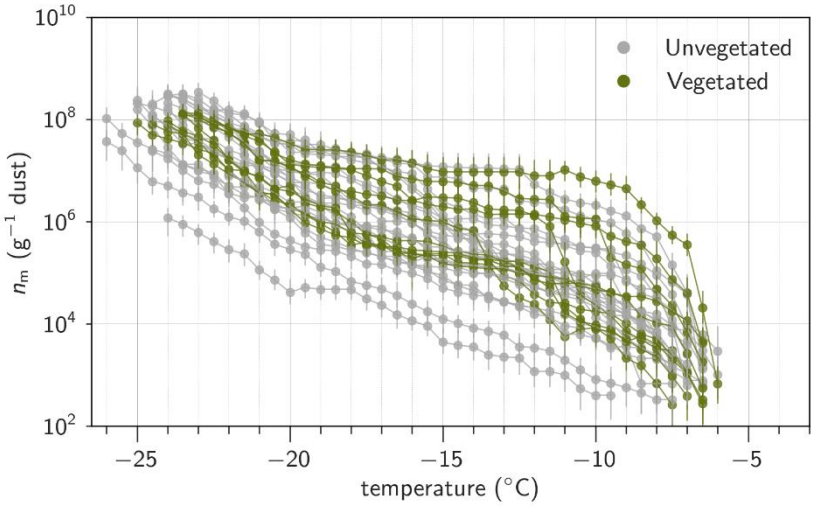

Figure S5. Ice-active site densities per mass (n_m) for unvegetated and vegetated samples. Note that all *transect* samples are unvegetated and only some *microbiology* samples are vegetated.

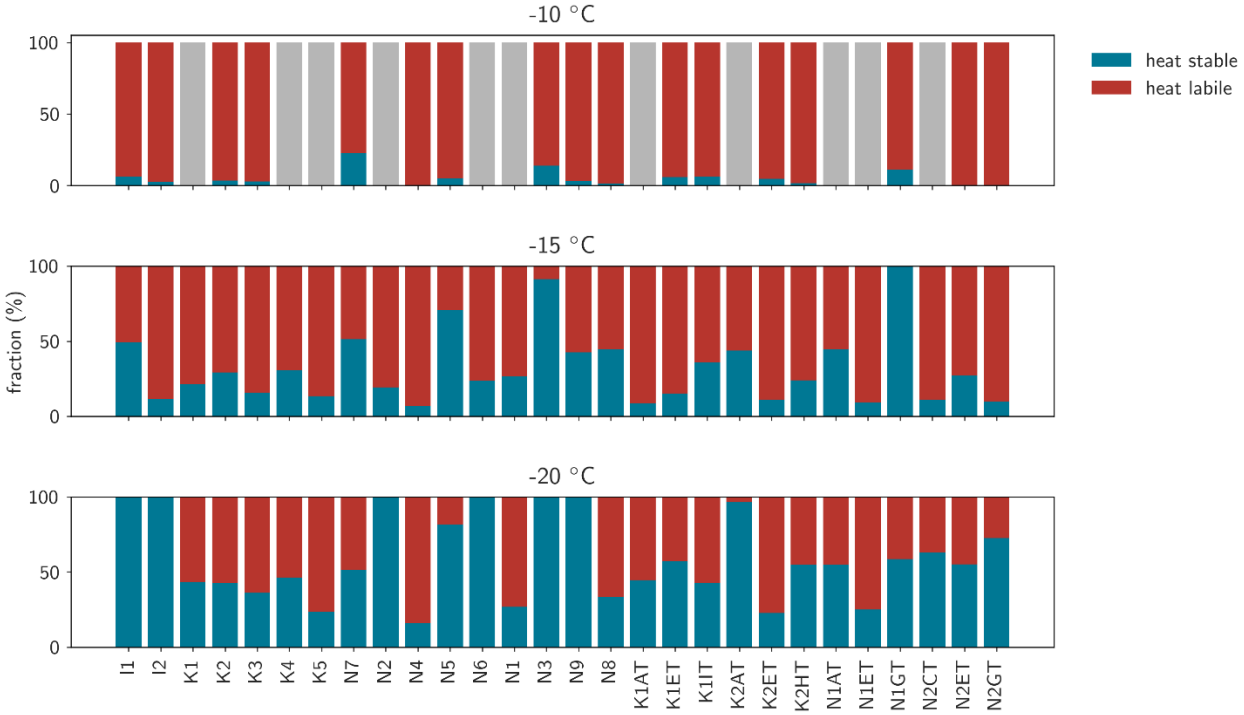

Figure S6. Heat labile and heat stable fractions. Heat labile and heat stable fraction at (a) -10 °C, (b) -15 °C, and (c) -20 °C. Grey bars indicate no data, but are likely primarily heat labile INPs**.** Fractions are calculated from the ratio of heat-treated to untreated INP concentrations. Fractions are calculated from the ratio of heat-treated to untreated INP concentrations. In cases where heat treatment yielded higher INP concentrations than untreated samples (e.g., sample N1GT between -10.5 and -19.5 °C), values were set equal to prevent negative heat-labile fractions.

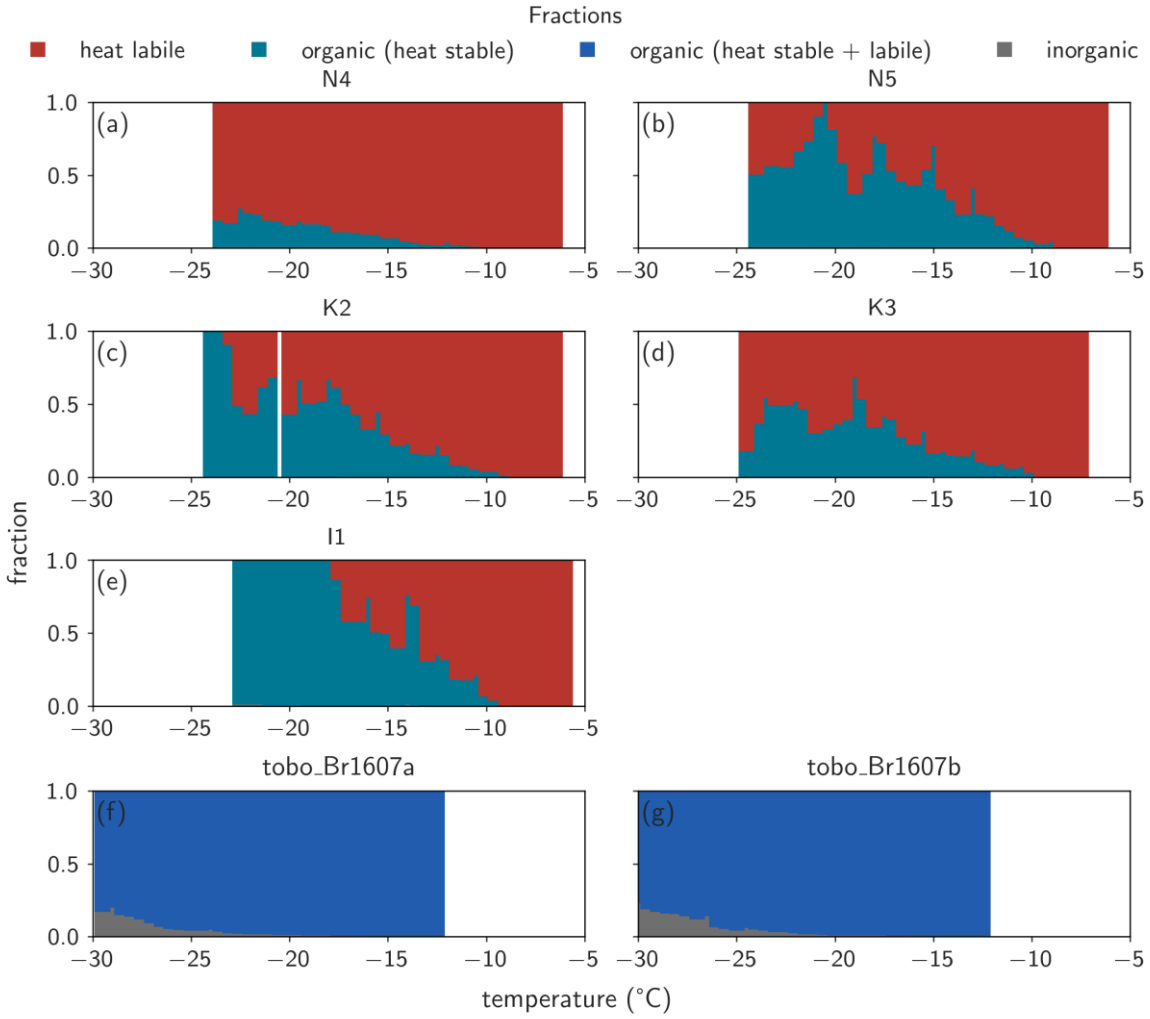

Figure S7. Composition information. Fraction of heat labile, organic (heat stable but peroxide sensitive), and inorganic (peroxide resistant) INPs per gram of dust for samples in Narsarsuaq (a, b), Kangerlussuaq (c, d), and Igaliku (e). Sample examples shown were selected without specific criteria. The inorganic fractions are too small to be visible in panels a-e. Panels (f) and (g) show the fraction of organic (which includes both heat labile and heat stable organics) and inorganic INPs per gram of dust for samples from Svalbard (Tobo et al., 2019). Fractions are calculated as: heat labile = (n_m - $n_{m,\,heat}$)/n_m, organic = ($n_{m,\,heat}$ - $n_{m,\,H2O2}$)/n_m, and inorganic = $n_{m,\,H2O2}$/n_m, where n_m, $n_{m,\,heat}$, and $n_{m,\,H2O2}$ represent untreated, heat treated, and hydrogen peroxide treated samples, respectively.

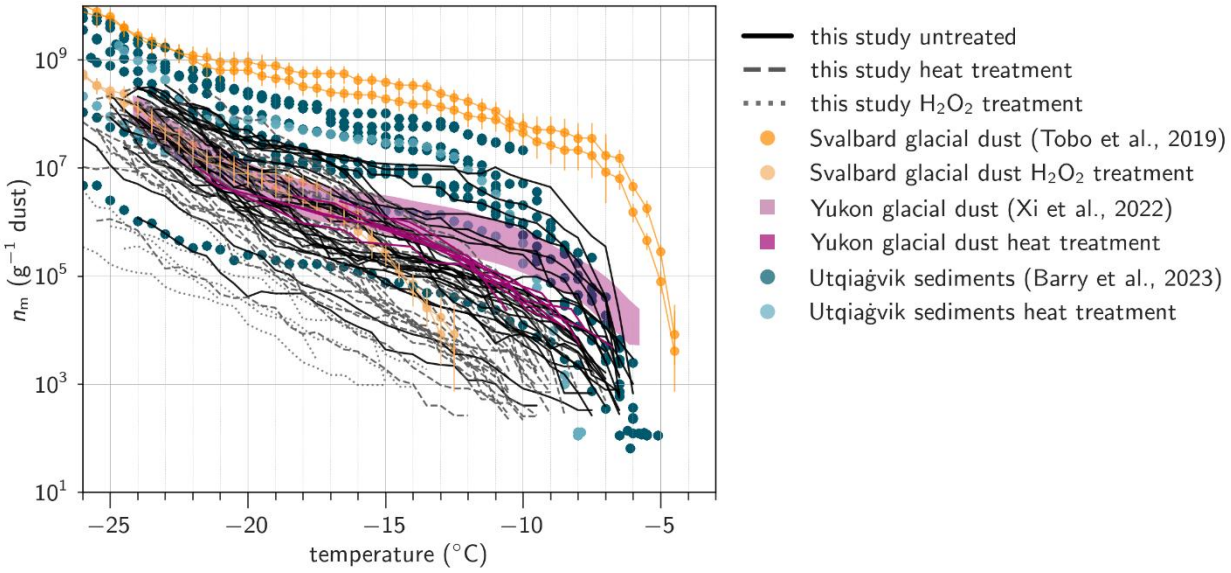

Figure S8. Literature comparison including heat and peroxide treatment. Ice-active site densities per mass (n_m) of bulk dust samples for this study without treatment, and including heat and peroxide treatment. Other high-latitude sites are added including untreated and hydrogen peroxide treated bulk dust samples by Tobo et al. (2019), untreated and heat treated (heating to 100 °C for 1 h) dust aerosol samples by Xi et al. (2022), and untreated and heat treated (heating to 95 °C for 20 min) sediment samples by Barry et al. (2023).

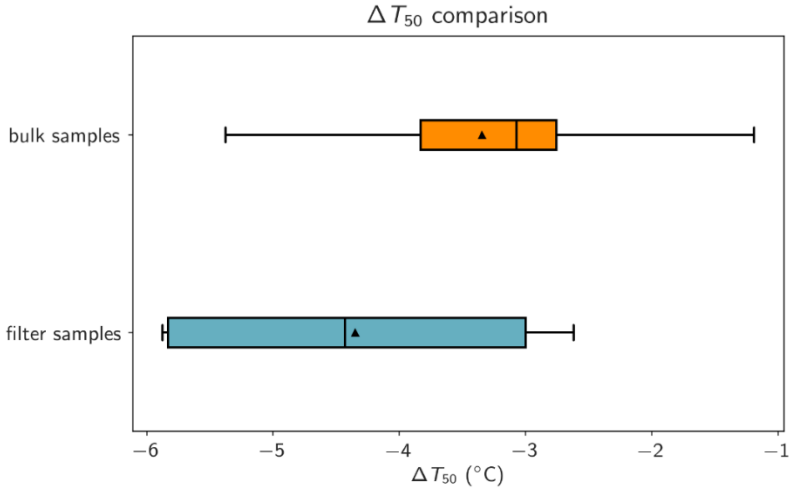

Figure S9. ΔT_{50} comparison. Difference of median freezing temperature T_{50} (temperature where 50 % of droplets are frozen) for the untreated and heat treated initial suspension (undiluted).

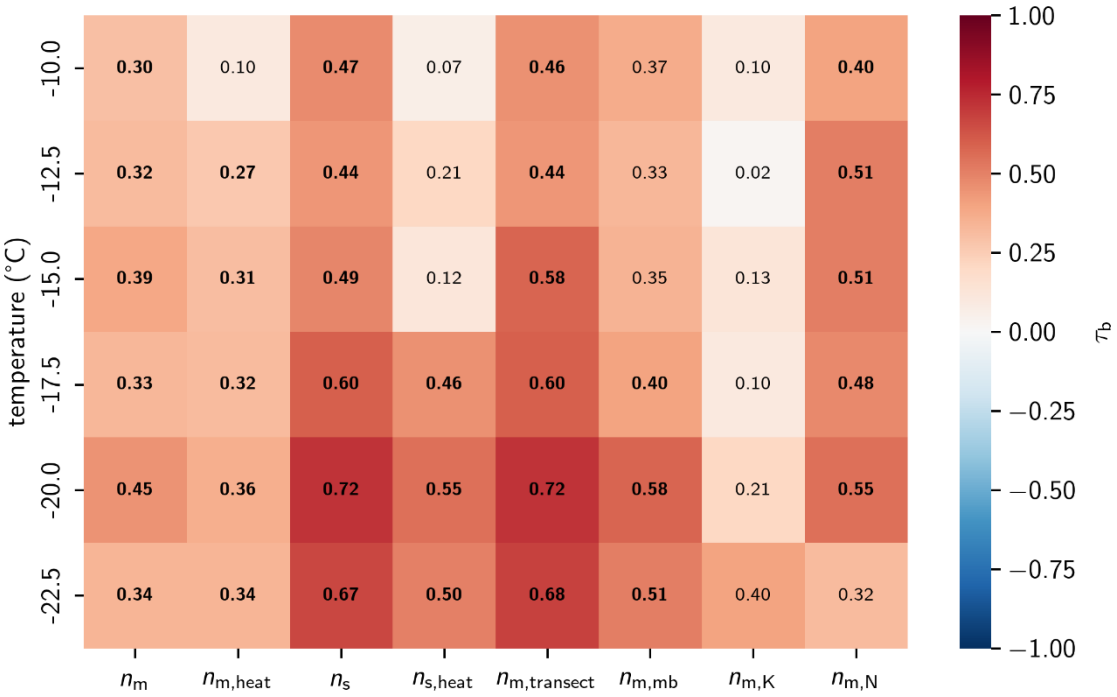

Figure S10. Correlation coefficient TOC and different variables. Kendall's tau correlation coefficient (τ_b) of total organic carbon (TOC) and ice-active site densities for different sample subsets and treatments, including ice-active site densities per mass (n_m) for all samples, n_m following heat treatment ($n_{m,heat}$), ice-active site densities per surface area (n_s), n_s following heat treatment ($n_{s,heat}$), n_m of *transect* samples ($n_{m,transect}$), n_m of *microbiology* samples ($n_{m,mb}$), n_m in Kangerlussuaq ($n_{m,K}$), and n_m in Narsarsuaq ($n_{m,N}$). The correlation coefficient is written in bold when statistically significant ($p < 0.05$).

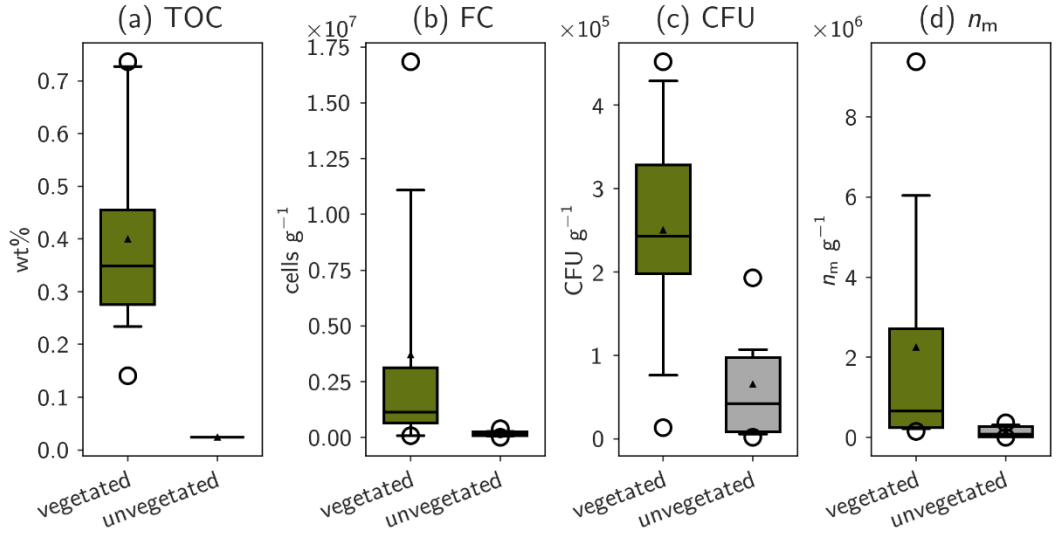

Figure S11. Influence of vegetation. Comparison of (a) TOC, microbial abundance based on (b) flow cytometry (FC) and (c) colony forming units (CFU), and (d) ice-active site densities per mass (n_m) at -15 °C for vegetated (n=10) and unvegetated (n=6) *microbiology* samples. Box plots show the median (center line), first and third quartiles (box edges), and whiskers extending to the 5th and 95th percentiles; outliers beyond this range are shown as individual points. The mean is marked by the black triangles.

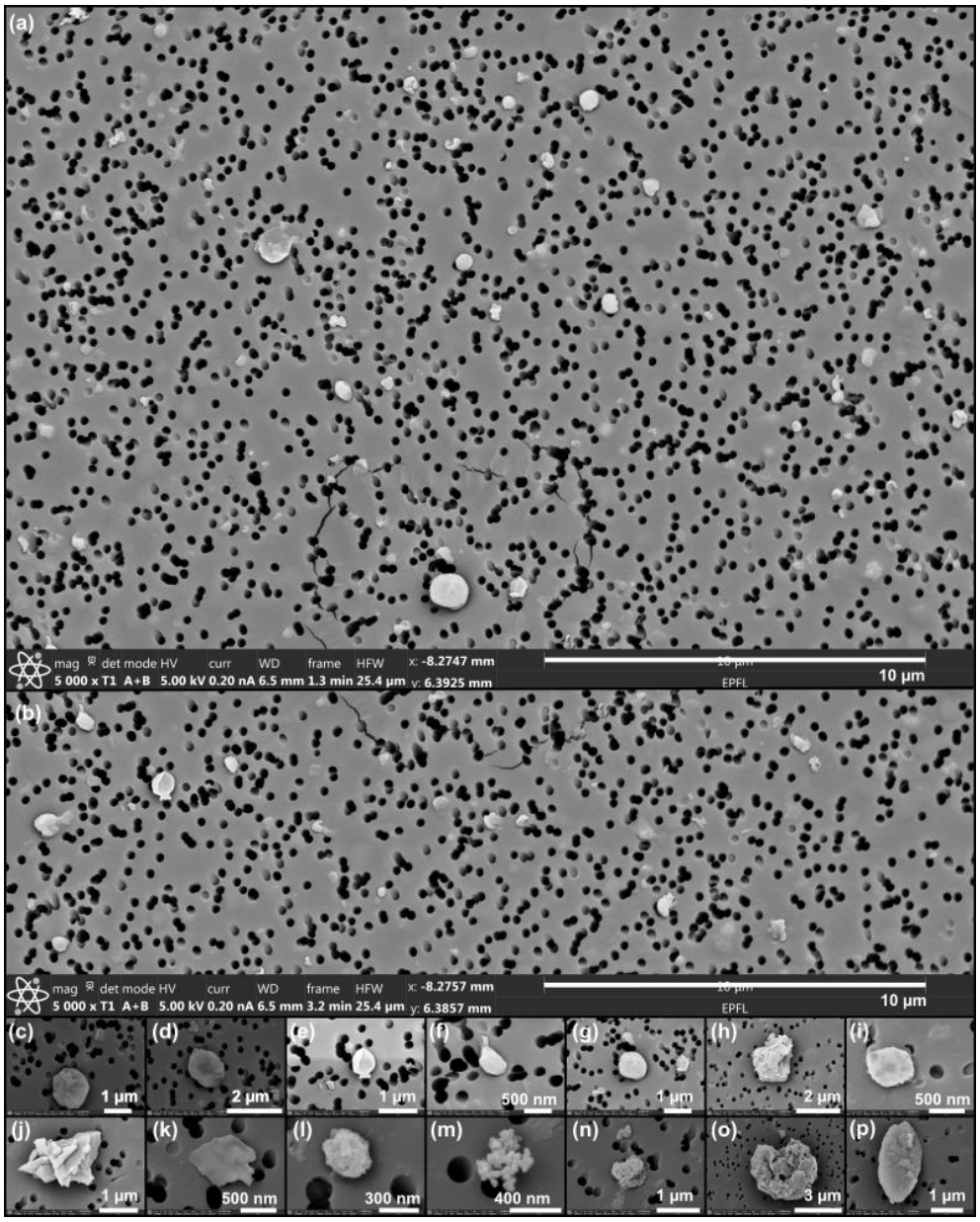

Figure S12. Images of aerosol particles at Narsarsuaq *plain* site. Scanning Electron Microscopy (SEM) images of aerosol particles on Nuclepore™ polycarbonate filters (0.2 µm pore diameter) sampled at the Narsarsuaq *plain* site from 22.06.2023 12:20 – 23.06.2023 13:10 (a-g) and 16.06.2023 13:03 – 17.06.2023 11:12 (h-p). Filters were coated with a 7 nm iridium layer prior to analysis to prevent charge accumulation analyzed with a Teneo® field-emission scanning electron microscope (FEI/Thermo Fisher Scientific, USA). (a, b) Overview images, manual counting in both overview images yielded ~135 particles, of which approximately 17 (~12%) were coarse-mode (> 0.5 µm). The remaining ~88% are fine-mode (< 0.5 µm) particles; note that fine-mode particles are likely underestimated due to detection limitations at this magnification, meaning the true coarse-mode fraction is probably lower. (c–g) Close-up images of particles from the same filter as (a, b), and (h–p) from the other filter. The majority display irregular, angular to sub-rounded morphology consistent with mineral dust, including platy sheet-like forms indicative of clay minerals. A minority show smoother, more rounded morphology potentially attributable to marine origin (such as in m). SEM EDX elemental analysis of a particle subset confirmed the presence of silicate minerals, consistent with mineral dust from the glacial outwash plain.

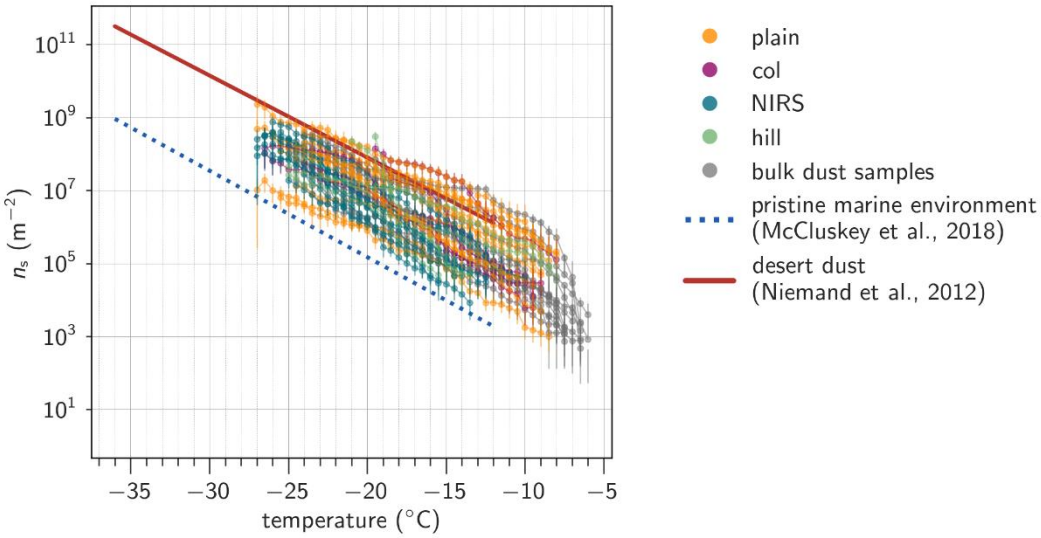

Figure S13. INP spectra normalized by surface area. Atmospheric INP concentrations normalized by the total aerosol surface area for particles larger than ≈190 nm, derived from optical particle counter measurements (Sect. 2.1.2). For comparison, INP spectra of bulk *transect* samples normalized by geometric surface area are shown, together with parameterizations for a pristine marine environment from measurements in the Southern Ocean **(McCluskey et al., 2018)** and desert dust (Niemand et al., 2012).

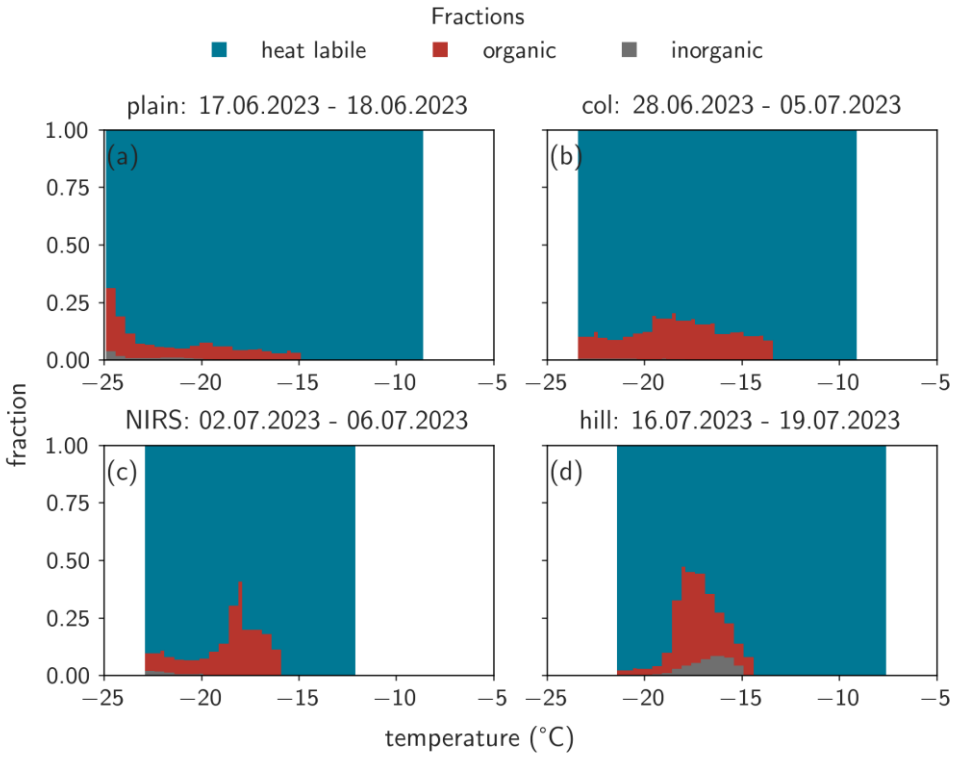

Figure S14. Composition information of filter samples. Fraction of heat labile, organic (heat stable but peroxide sensitive), and inorganic (peroxide resistant) INPs for a filter sample at the (a) Narsarsuaq plain, (b) Narsarsuaq col, (c) Narsaq International Research Station (NIRS), and (d) Tasigaaq hill near Narsaq. The sampling period of each filter is indicated in the title. Fractions are calculated as: heat labile = (n_m - $n_{m,\,heat}$)/n_m, organic = ($n_{m,\,heat}$ - $n_{m,\,H2O2}$)/n_m, and inorganic = $n_{m,\,H2O2}$/n_m, where n_m, $n_{m,\,heat}$, and $n_{m,\,H2O2}$ represent untreated, heat treated, and hydrogen peroxide treated samples, respectively.

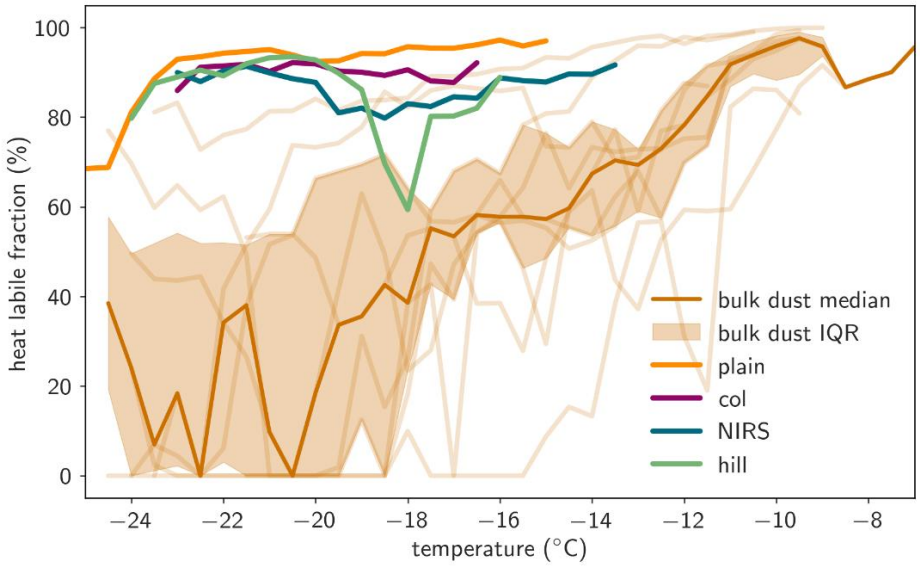

Figure S15. Heat labile fractions. Heat labile fractions of Narsarsuaq bulk dust samples (including median and IQR) and aerosol filter samples for the different locations as a function of temperature. The light brown lines represent the heat labile fractions of individual bulk dust samples.

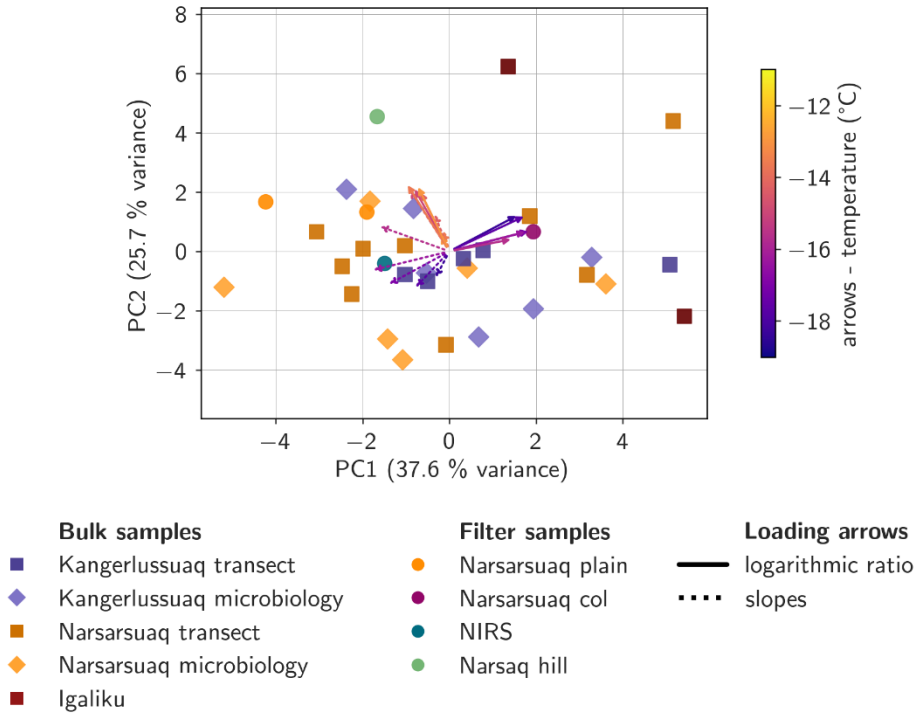

Figure S16. Variability in heat treated INP spectra. Principal component analysis (PCA) for all samples, based on the slopes of heat treated INP spectra in 2 °C intervals from -10 °C to -20 °C, and the logarithmic ratios of INP concentrations at each interval relative to -15°C. The arrows represent the variable loadings, color-coded by temperature, where solid arrows indicate the logarithmic ratios, dotted arrows represent the slopes. Axes represent the first two principal components scaled to the variance explained.

S2. Temporal INP variability

To identify potential sources of atmospheric INPs, we assess the temporal variability in combination with coarse-mode aerosol and meteorological variables in Fig. S17. The highest coarse-mode aerosol concentrations (> 0.5 µm d_{opt}) at the different sites coincided with the transport of biomass-burning plumes from Canadian wildfires (Fig. S17d,e) (Alden et al., 2025). However, despite high aerosol concentrations, the INP concentrations during these periods were typically not higher than during other times (Fig. S17a,b,c, Fig. S18, with exception at the hill site for plume 3), suggesting that the transported plumes had low INP content. Biomass burning aerosols as INPs in the immersion-mode (Adams et al., 2020) and tend to activate only at colder temperatures (approximately < -30°C, Kanji et al., 2017), though they have been shown to contribute to INPs (Petters et al., 2009; Pratt et al., 2011; Twohy et al., 2010). Specifically, ship-borne observations over the western North Pacific and Arctic Ocean suggest that particles originating from boreal wildfires can significantly contribute to INP concentrations across a range of temperatures (-15 to -25°C; Taketani et al., 2025). The differences in INP efficiencies influenced by biomass burning plumes may reflect variations in burning conditions, fuel type, or the mixing state of emitted particles during transport.

No clear relationship emerged between meteorological variables, air mass trajectories, and the ambient INP concentrations (though such links may have been obscured by the long and/or variable sampling durations). For most of the campaign, weather conditions were sunny, dry and calm, and air masses came predominantly from the southwestern direction (Fig. S19). The only high-wind speed Foehn event (28-20 July 2023, wind speeds up to 12.5 m s^{-1} at *plain* and 14.8 m s^{-1} at *col*) did not lead to increased coarse-mode aerosol number concentrations, nor INP concentrations (Fig. S17a-e, Fig. S20). Possibly, dust emissions were limited by elevated soil moisture, which can increase particle cohesion and raise the threshold wind velocity for soil erosion. However, estimates based on Fécan et al. (1999) using measured soil moisture at the *plain* site and different soil densities (not measured) would suggest that the wind speed threshold velocity for soil erosion was exceeded (Fig. S21). Additionally, dust emissions could have been limited by the presence of biological crusts on soil surfaces, which are known to efficiently suppress wind erosion (e.g., Gao et al., 2017) and have been observed at several of the sampling sites (Fig. S2).

Bioaerosols and INPs have previously been observed to increase during and after precipitation (Conen et al., 2017; Huffman et al., 2013), and observations from northern Finland reported a positive correlation between the abundance of fluorescent particles indicative of fungal spores and relative humidity during summer and autumn, suggesting humidity-driven fungal spore release mechanisms that could contribute to INPs (Gratzl et al., 2025). In our dataset, some spectra with elevated high-temperature INP concentrations occurred during precipitation events (Fig. S22), and the negative correlation between high-temperature INPs and air temperature (Fig. S23) may hint at enhanced biological emissions under the cooler conditions surrounding precipitation events. However, meteorological variables, including precipitation and humidity, do not show a consistent pattern with INP variability across the campaign.

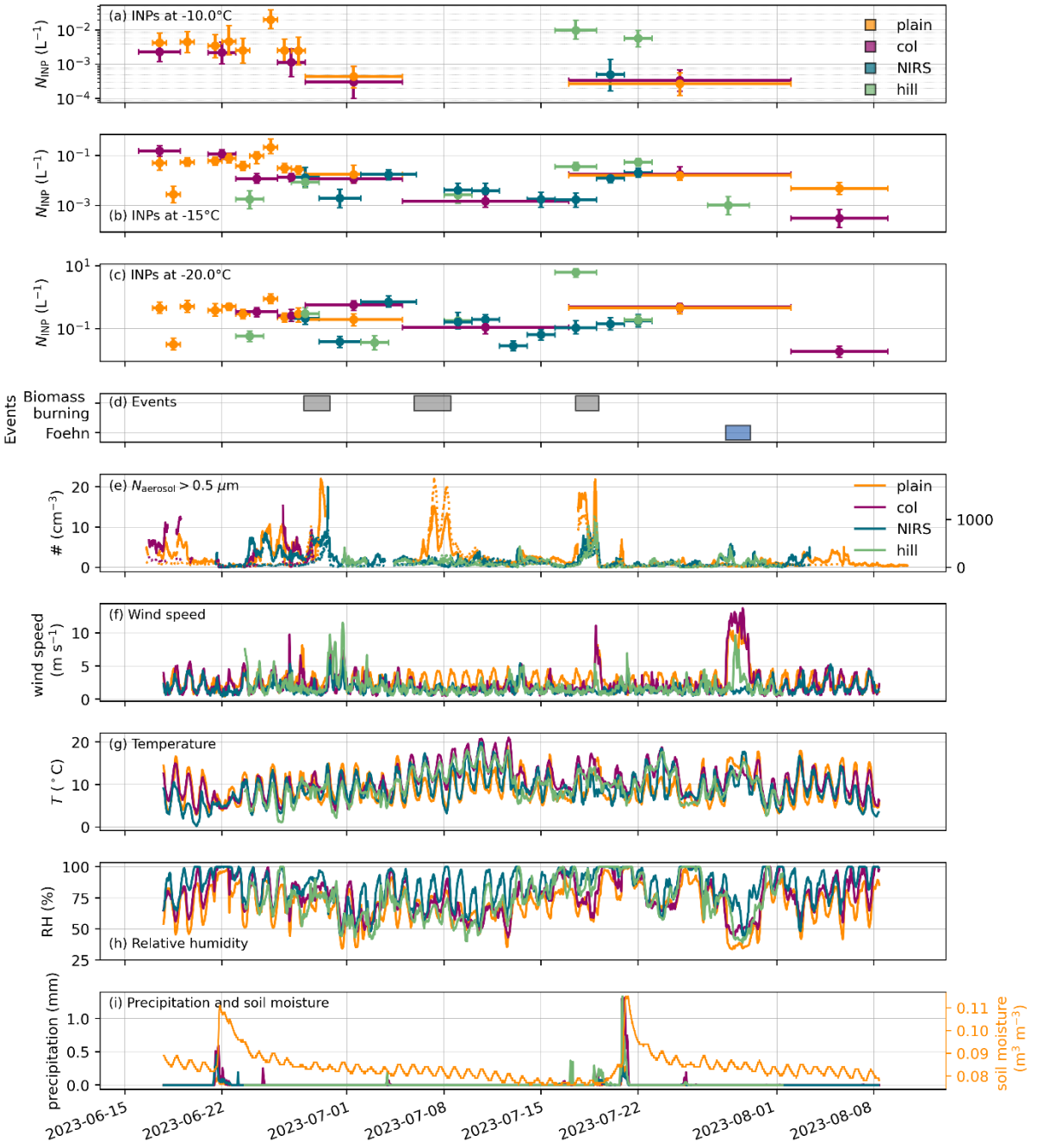

Figure S17. Time series of INPs, coarse particles and meteorology. INP concentrations at (a) -10 °C, (b) -15 °C, and (c) -20 °C, the colored horizontal lines indicate the filter sampling period, the vertical errorbars indicate the 95 % confidence intervals. Where INP data is shown for -15 °C, but not for -20 °C, the activated fraction reached the detection limit of the performed dilutions; no extrapolation beyond the last reliable data point is shown. (d) Time periods of events including biomass burning plumes transported from Canada, and a Foehn event. (e) Particle number concentration > 0.5 µm, (f) 2 m wind speed, (g) temperature, (h) relative humidity, (i) precipitation and soil moisture at the different locations including Narsarsuaq plain (*plain*), Narsarsuaq col (*col*), Narsaq International Research station (*NIRS*), and Tasigaaq hill (*hill*) near Narsaq, distinguished by color (legend in panel e). Soil moisture is only measured at the Narsarsuaq *plain* site.

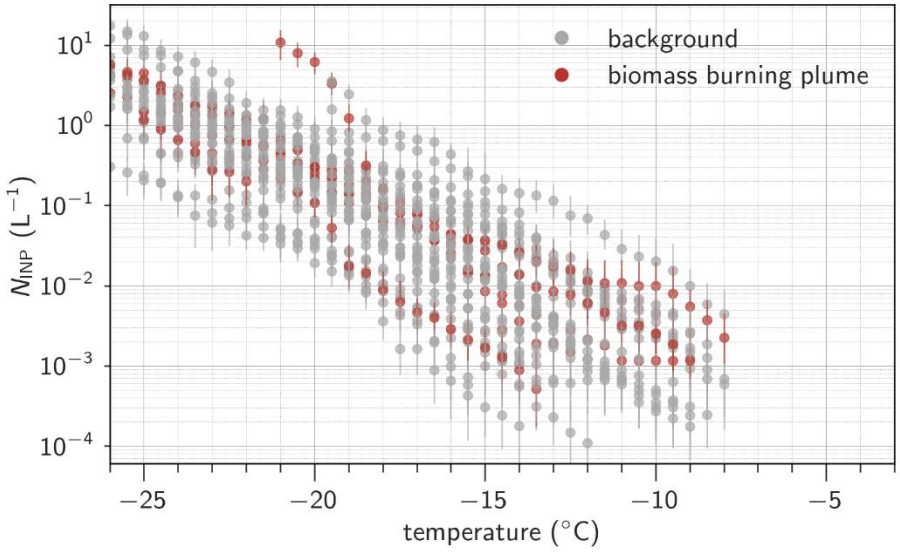

Figure S18. Biomass burning plume. INP spectra with filters during biomass burning plumes marked in red.

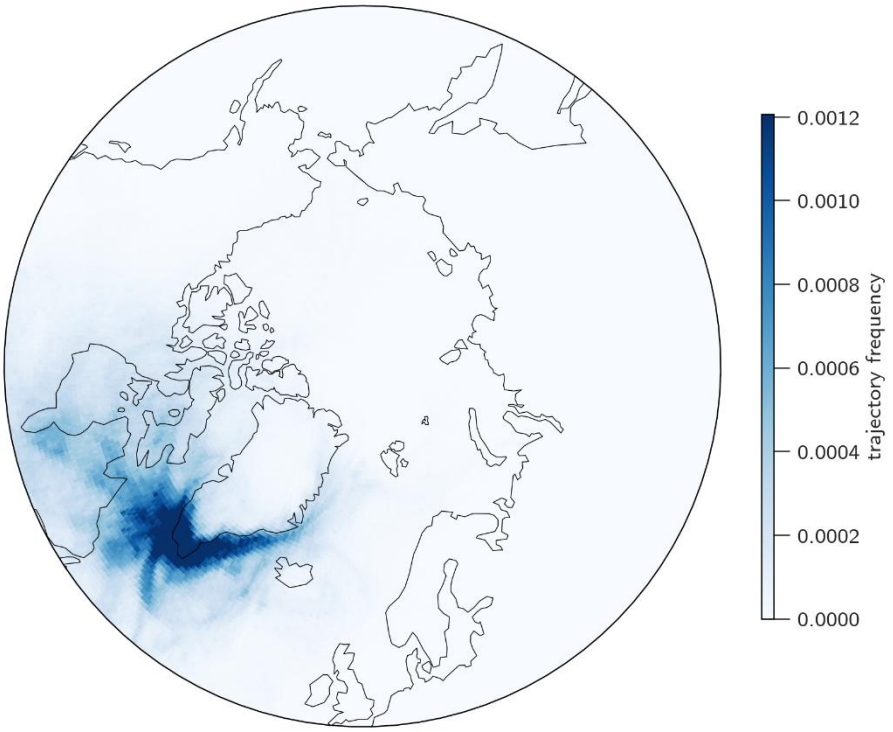

Figure S19. Trajectory frequency. Relative frequency of 5-day backward trajectories (Lagranto, Sprenger and Wernli, 2015) initialized near the surface at Narsaq at 3-hour intervals between 16.06.2023 – 02.08.2023 using ERA5 meteorology.

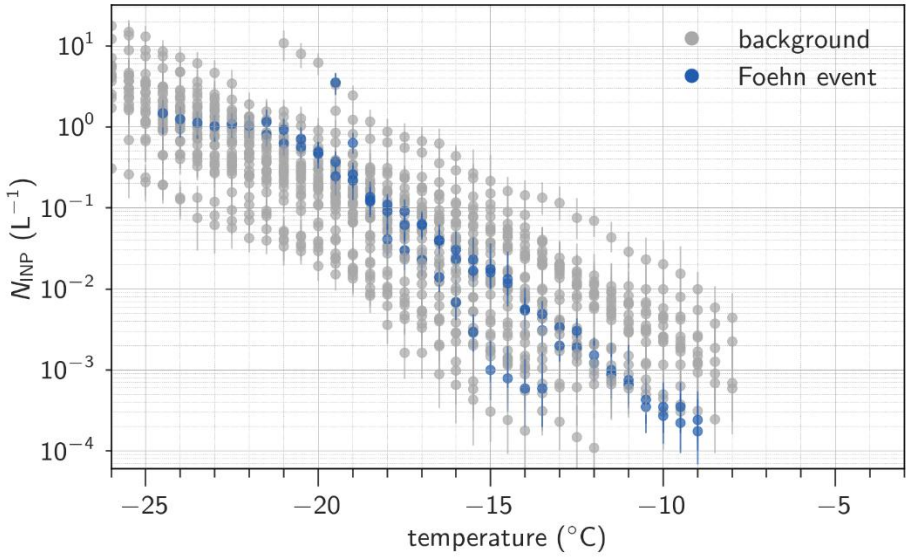

Figure S20. Foehn event. INP spectra with filters during Foehn event marked in blue.

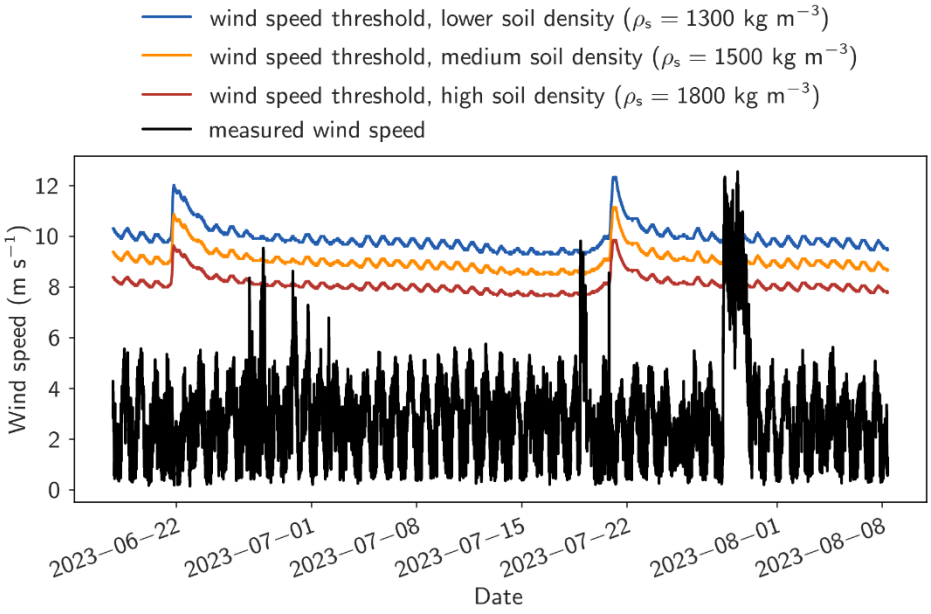

Figure S21. Wind speed threshold for dust emission. Wind speed threshold estimates are based on Fig. 3 in Fécan et al. (1999). Measured volumetric soil moisture at the plain station was converted to gravimetric soil moisture assuming different soil densities (colored lines), measured wind speed at the Narsarsuaq plain station is shown in black.

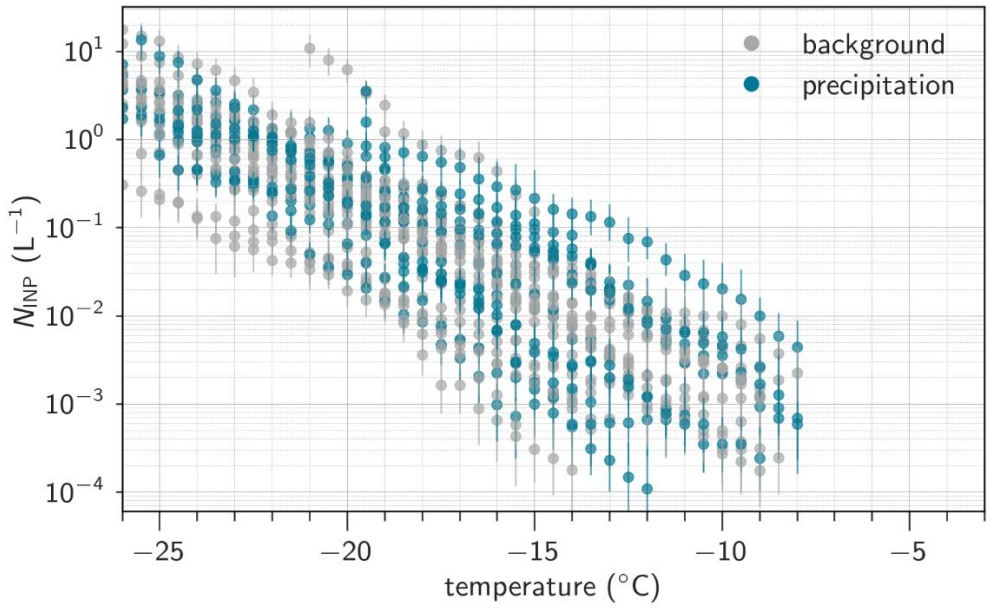

Figure S22. Precipitation. INP spectra with filters during precipitation during the sampling period marked in blue.

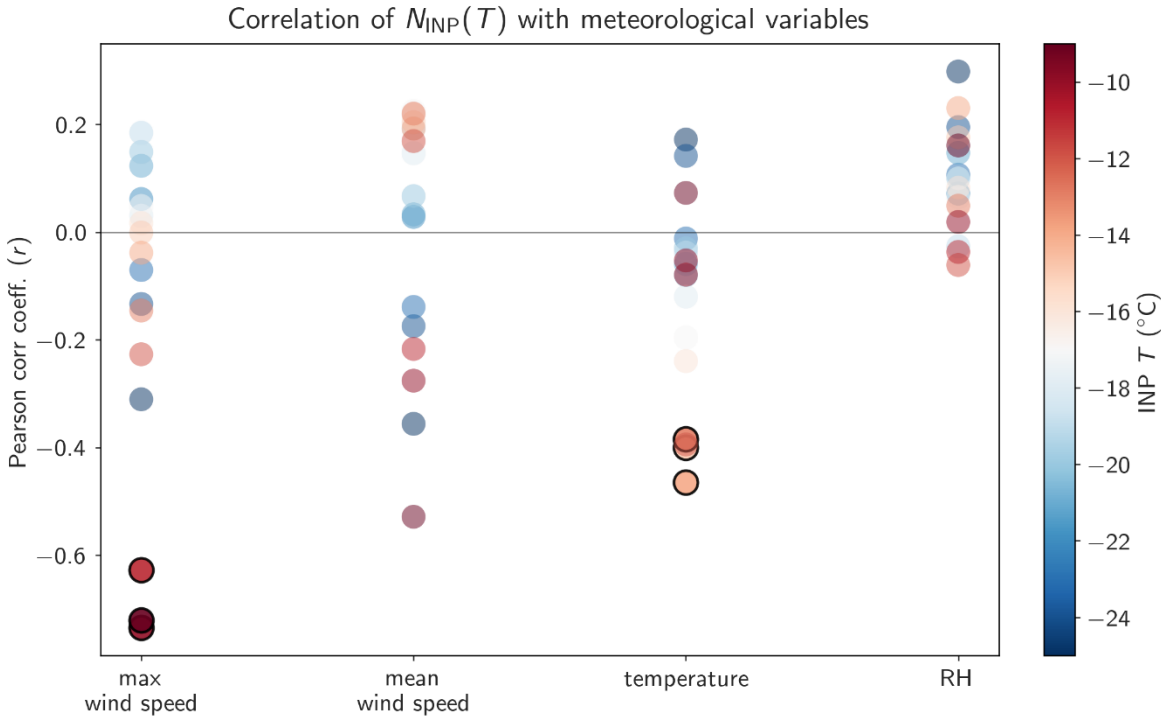

Figure S23. Correlation of N_{INP} and meteorological variables. Pearson correlation coefficient of atmospheric INP concentrations (N_{INP}) with maximum and mean wind speed during the filter period, mean temperature, and relative humidity (RH) at all atmospheric stations.

S3. INPs in glacial outwash plains in the Swiss Alps

To compare the ice-nucleating properties of glacial dust from Greenland with those from other glaciated regions, we additionally collected dust samples from three glacial outwash plains in the Swiss Alps (canton of Valais, southwestern Switzerland). Although the Alpine outwash plains are considerably smaller in extent and are unlikely to represent a major regional INP source, the underlying processes governing dust generation and composition may be comparable to those in Greenland. Samples were collected along transects at each site, as summarized in Table S1 and shown in Fig. S24. Sample preparation and INP measurements were conducted following the same procedures as for the Greenland *transect* samples, described in Sect. 2.1.1 and Sect. 2.2.

Table S4. Overview of bulk dust samples.

Location	ID	Latitude (°)	Longitude (°)	Date (YYYY-MM-DD)	INP treatments
Lämmerenboden	L1	46.3969735	7.6026584	2025-07-02	heat, H_2O_2
	L2a	46.3968498	7.5998052	2025-07-02	
	L2b	46.3968498	7.5998052	2025-07-02	
	L3	46.39613	7.59511	2025-07-02	
Lac du Grand	LG1	46.5157812	7.20105486	2025-07-11	
Désert	LG2	46.0860320	7.3373169	2025-07-11	heat, H_2O_2
	LG3	46.0784114	7.3379723	2025-07-11	
	LG4	46.0761233	7.338429	2025-07-11	
Ferpècle	F1	46.0445107	7.5539348	2025-07-04	
	F2	46.0460984	7.5536347	2025-07-04	heat, H_2O_2
	F3	46.0473208	7.5527398	2025-07-04	
	F4	46.0484822	7.5532675	2025-07-04	

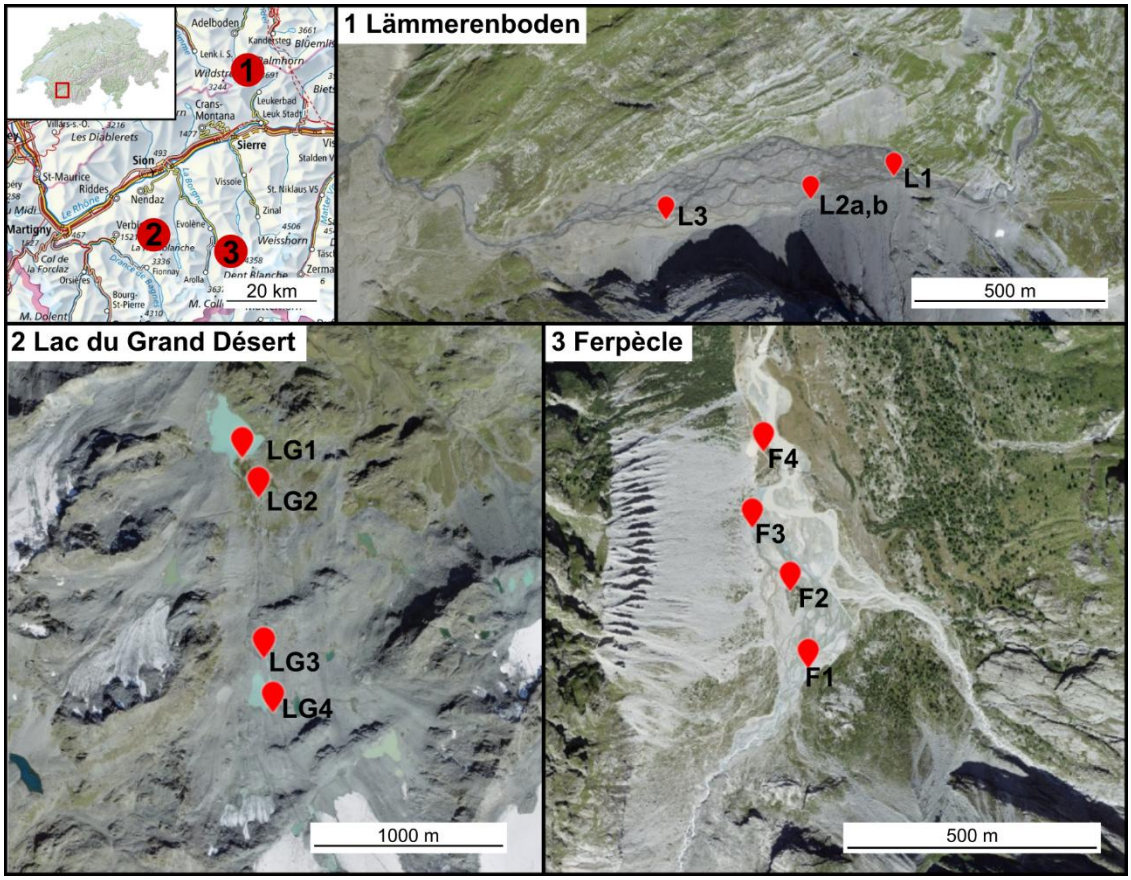

Figure S24. Map of sampling locations in the Swiss Alps. Maps and aerial images are from the Federal Office of Topography swisstopo.

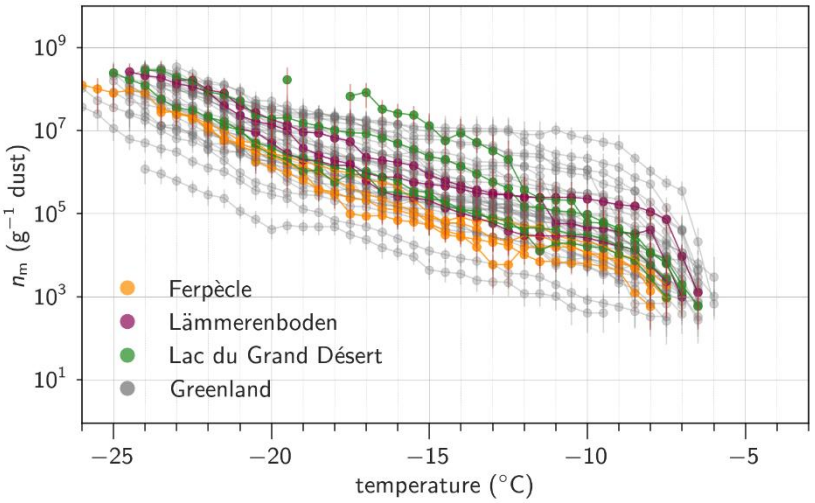

Figure S25. Bulk dust ice-nucleating activity. Ice-active site densities per mass (n_m) of dust samples in glacial outwash plains in the Swiss Alps (Ferpècle, Lämmerenboden, Lac du Grand Désert) and Greenland.

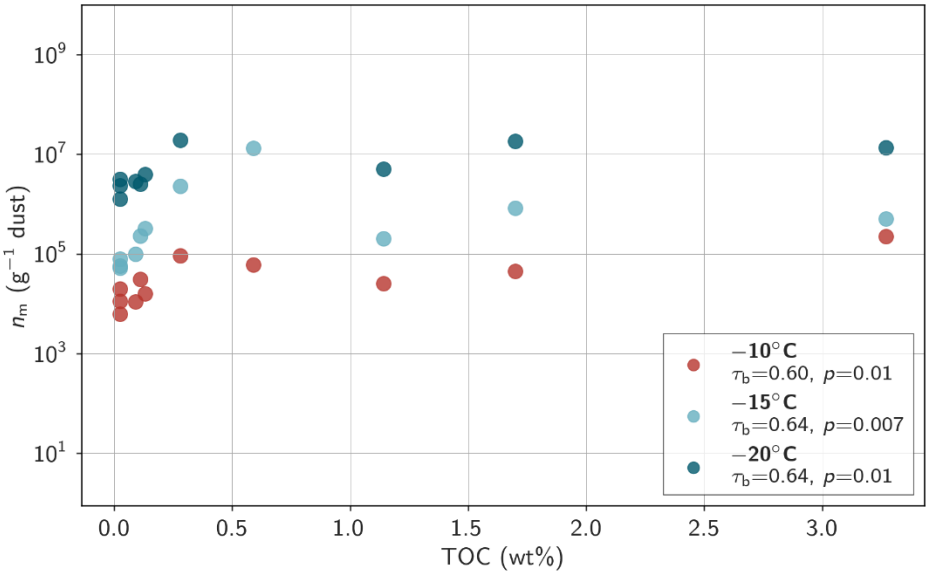

Figure S26. TOC and ice-nucleating activity. Scatterplot of total organic carbon (TOC) content vs ice-active site densities per mass (n_m) for the temperatures -10 °C, -15 °C, and -20 °C. For each temperature, Kendall's tau correlation coefficient (τ_b) and p-value are annotated.

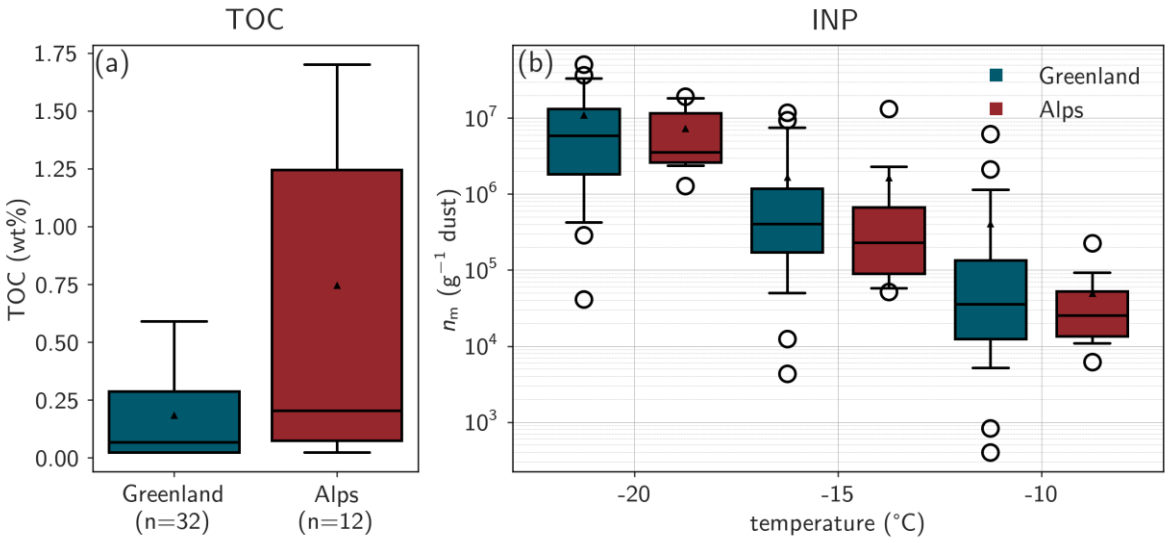

Figure S27. Comparison TOC and INPs. Comparison of (a) TOC values and (b) ice-active site densities per mass (n_m) at -20 °C, -15 °C, and -10 °C between dust samples from glacial outwash plains in Greenland and the Swiss Alps. Box plots show the median (center line), first and third quartiles (box edges), and whiskers extending to the 5th and 95th percentiles; outliers beyond this range are shown as individual points. The mean is marked by the black triangles.

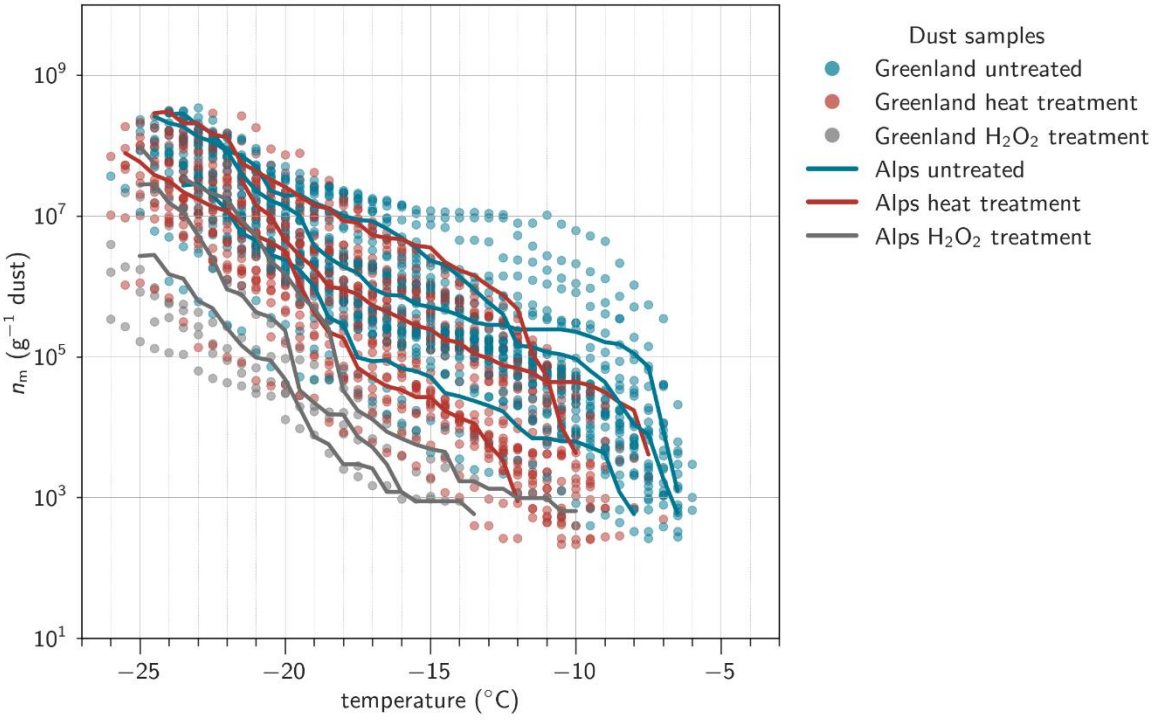

Figure S28. INP composition of dust samples. n_m spectra of bulk dust sample including heat and hydrogen peroxide treatment from glacial outwash plains in Greenland and the Swiss Alps.

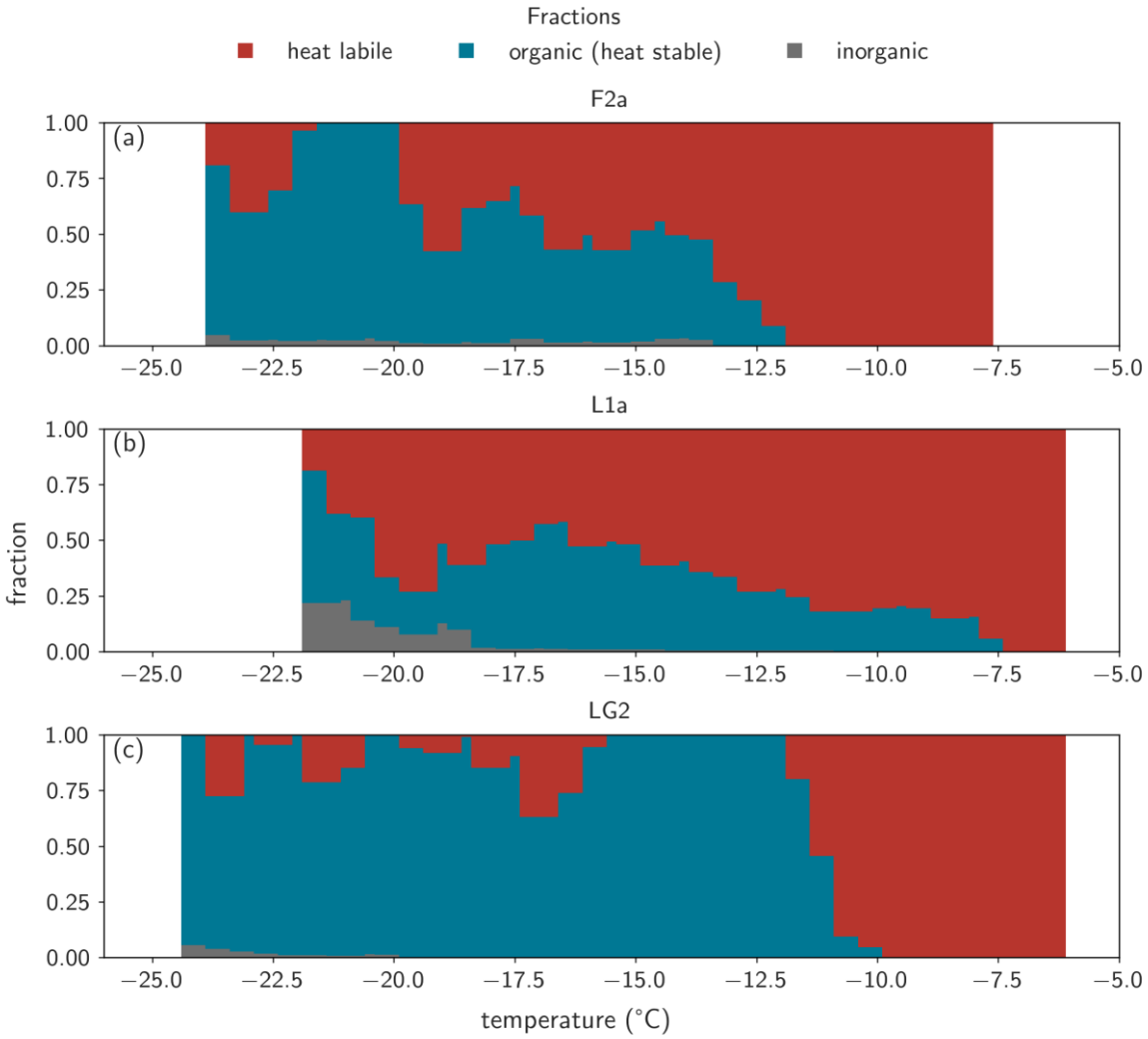

Figure S29. Composition information. Fraction of heat labile, organic (heat stable but peroxide sensitive), and inorganic INPs per gram of dust for samples from (a) Ferpècle, (b) Lämmerenboden, and (c) Lac du Grand Désert (Swiss Alps). Fractions are calculated as: heat labile = (n_m - $n_{m,\,heat}$)/n_m, organic = ($n_{m,\,heat}$ - $n_{m,\,H2O2}$)/n_m, and inorganic = $n_{m,\,H2O2}$/n_m, where n_m, $n_{m,\,heat}$, and $n_{m,\,H2O2}$ represent untreated, heat treated, and hydrogen peroxide treated samples, respectively.

References

Adams, M. P., Tarn, M. D., Sanchez-Marroquin, A., Porter, G. C. E., O'Sullivan, D., Harrison, A. D., Cui, Z., Vergara-Temprado, J., Carotenuto, F., Holden, M. A., Daily, M. I., Whale, T. F., Sikora, S. N. F., Burke, I. T., Shim, J.-U., McQuaid, J. B., and Murray, B. J.: A Major Combustion Aerosol Event Had a Negligible Impact on the Atmospheric Ice-Nucleating Particle Population, Journal of Geophysical Research: Atmospheres, 125, e2020JD032938, https://doi.org/10.1029/2020JD032938, 2020.

Alden, J., Bergner, N., Heutte, B., Favre, L., Surdu, M., Weng, J., Augugliaro, M., Winiger, P., Dönmez, B., Pohorsky, R., Calmer, R., Chatterjee, C., Violaki, K., Nenes, A., Gregor, L., Henning, S., and Schmale, J.: Vertically-resolved source contributions to climate-relevant aerosol properties in Southern Greenlandic fjord systems, EGUsphere, 1–43, https://doi.org/10.5194/egusphere-2025-5710, 2025.

Barry, K. R., Hill, T. C. J., Nieto-Caballero, M., Douglas, T. A., Kreidenweis, S. M., DeMott, P. J., and Creamean, J. M.: Active thermokarst regions contain rich sources of ice-nucleating particles, Atmospheric Chemistry and Physics, 23, 15783–15793, https://doi.org/10.5194/acp-23-15783-2023, 2023.

Conen, F., Eckhardt, S., Gundersen, H., Stohl, A., and Yttri, K. E.: Rainfall drives atmospheric ice-nucleating particles in the coastal climate of southern Norway, Atmospheric Chemistry and Physics, 17, 11065–11073, https://doi.org/10.5194/acp-17-11065-2017, 2017.

Fécan, F., Marticorena, B., and Bergametti, G.: Parametrization of the increase of the aeolian erosion threshold wind friction velocity due to soil moisture for arid and semi-arid areas, Annales Geophysicae, 17, 149–157, https://doi.org/10.1007/s00585-999-0149-7, 1999.

Gao, L., Bowker, M. A., Xu, M., Sun, H., Tuo, D., and Zhao, Y.: Biological soil crusts decrease erodibility by modifying inherent soil properties on the Loess Plateau, China, Soil Biology and Biochemistry, 105, 49–58, https://doi.org/10.1016/j.soilbio.2016.11.009, 2017.

Gratzl, J., Böhmländer, A., Pätsi, S., Pogner, C.-E., Gorfer, M., Brus, D., Doulgeris, K. M., Wieland, F., Asmi, E., Saarto, A., Möhler, O., Stolzenburg, D., and Grothe, H.: Locally emitted fungal spores serve as high-temperature ice nucleating particles in the European sub-Arctic, Atmospheric Chemistry and Physics, 25, 12007–12035, https://doi.org/10.5194/acp-25-12007-2025, 2025.

Huffman, J. A., Prenni, A. J., DeMott, P. J., Pöhlker, C., Mason, R. H., Robinson, N. H., Fröhlich-Nowoisky, J., Tobo, Y., Després, V. R., Garcia, E., Gochis, D. J., Harris, E., Müller-Germann, I., Ruzene, C., Schmer, B., Sinha, B., Day, D. A., Andreae, M. O., Jimenez, J. L., Gallagher, M., Kreidenweis, S. M., Bertram, A. K., and Pöschl, U.: High concentrations of biological aerosol particles and ice nuclei during and after rain, Atmospheric Chemistry and Physics, 13, 6151–6164, https://doi.org/10.5194/acp-13-6151-2013, 2013.

Kanji, Z. A., Ladino, L. A., Wex, H., Boose, Y., Burkert-Kohn, M., Cziczo, D. J., and Krämer, M.: Overview of Ice Nucleating Particles, Meteorological Monographs, 58, 1.1-1.33, https://doi.org/10.1175/AMSMONOGRAPHS-D-16-0006.1, 2017.

McCluskey, C. S., Hill, T. C. J., Humphries, R. S., Rauker, A. M., Moreau, S., Strutton, P. G., Chambers, S. D., Williams, A. G., McRobert, I., Ward, J., Keywood, M. D., Harnwell, J., Ponsonby, W., Loh, Z. M., Krummel, P. B., Protat, A., Kreidenweis, S. M., and DeMott, P. J.: Observations of Ice Nucleating Particles Over Southern Ocean Waters, Geophysical Research Letters, 45, 11,989-11,997, https://doi.org/10.1029/2018GL079981, 2018.

Niemand, M., Möhler, O., Vogel, B., Vogel, H., Hoose, C., Connolly, P., Klein, H., Bingemer, H., DeMott, P., Skrotzki, J., and Leisner, T.: A Particle-Surface-Area-Based Parameterization of Immersion Freezing on Desert Dust Particles, Journal of the Atmospheric Sciences, 69, 3077–3092, https://doi.org/10.1175/JAS-D-11-0249.1, 2012.

Petters, M. D., Parsons, M. T., Prenni, A. J., DeMott, P. J., Kreidenweis, S. M., Carrico, C. M., Sullivan, A. P., McMeeking, G. R., Levin, E., Wold, C. E., Collett Jr., J. L., and Moosmüller, H.: Ice nuclei emissions from biomass burning, Journal of Geophysical Research: Atmospheres, 114, https://doi.org/10.1029/2008JD011532, 2009.

Pratt, K., Murphy, S., DeMott, P., Kok, G., Campos, T., Rogers, D., Prenni, A., Heymsfield, A., Seinfeld, J., and Prather, K.: Flight-based chemical characterization of biomass burning aerosols within two prescribed burn smoke plumes, Atmospheric Chemistry and Physics, 11, 12549–12565, https://doi.org/10.5194/acp-11-12549-2011, 2011.

Sprenger, M. and Wernli, H.: The LAGRANTO Lagrangian analysis tool – version 2.0, Geoscientific Model Development, 8, 2569–2586, https://doi.org/10.5194/gmd-8-2569-2015, 2015.

Taketani, F., Tobo, Y., Miyakawa, T., Takigawa, M., Zhu, C., and Kanaya, Y.: Impact of Siberian Wildfires on Ice-Nucleating Particle Concentrations over the Northwestern Pacific, Environ. Sci. Technol., 59, 2565–2574, https://doi.org/10.1021/acs.est.4c04889, 2025.

Tobo, Y., Adachi, K., DeMott, P. J., Hill, T. C. J., Hamilton, D. S., Mahowald, N. M., Nagatsuka, N., Ohata, S., Uetake, J., Kondo, Y., and Koike, M.: Glacially sourced dust as a potentially significant source of ice nucleating particles, Nat. Geosci., 12, 253–258, https://doi.org/10.1038/s41561-019-0314-x, 2019.

Twohy, C. H., DeMott, P. J., Pratt, K. A., Subramanian, R., Kok, G. L., Murphy, S. M., Lersch, T., Heymsfield, A. J., Wang, Z., Prather, K. A., and Seinfeld, J. H.: Relationships of Biomass-Burning Aerosols to Ice in Orographic Wave Clouds, Journal of the Atmospheric Sciences, 67, 2437–2450, https://doi.org/10.1175/2010JAS3310.1, 2010.

Xi, Y., Xu, C., Downey, A., Stevens, R., O. Bachelder, J., King, J., L. Hayes, P., and K. Bertram, A.: Ice nucleating properties of airborne dust from an actively retreating glacier in Yukon, Canada, Environmental Science: Atmospheres, 2, 714–726, https://doi.org/10.1039/D1EA00101A, 2022.